A Two-Step Projected Iterative Algorithm for Tropospheric Water Vapor Tomography

Shangyi Liu [ID], Kefei Zhang, Suqin Wu [ID], Wenyuan Zhang [ID], Longjiang Li, Moufeng Wan [ID], Jiaqi Shi, Minghao Zhang [ID], and Andong Hu

Abstract—The tropospheric tomography is an ill-posed inversion problem due to the sparsity of global navigation satellite systems (GNSS) stations and the limitation on the projection angles of GNSS signals, which in turn affects the stability and robustness of the tomographic solution. To address this, a new tomographic algorithm, named two-step projected iterative algorithm (TSPIA), is proposed. The wet refractivity (WR) field was constructed in two steps: first, an iterative preprocessing for the initial input values was performed, and then its resultant solution was input into the projected iterative method, in which a hypothesis convex set was constructed to constrain the reconstruction based on the classical algebraic iterative reconstruction (AIR) methods. In addition, a two-dimensional normalized cumulative periodogram (2-D-NCP) termination criterion was investigated since the traditional criteria for judging the convergence of iterations use prefixed empirical thresholds, which may lead to excessive iterations and need complicated work. The TSPIA was tested using GNSS data in Hong Kong over a wet period and a dry period. Statistical results showed that, compared to the classical AIR methods, the accuracy of the reconstructed WR field of the TSPIA were improved by about 10% and 15% when radiosonde and ECMWF data were used as the reference, respectively. Moreover, experiments for the proposed 2-D-NCP criterion demonstrated noticeable computational efficiency. These results suggest that the new approaches proposed in this article can improve the performance of the iterative methods for GNSS tropospheric tomography.

Index Terms—Algebraic reconstruction technique (ART), global navigation satellite systems (GNSS), ill-posed problem, projected iterative method, tropospheric tomography.

I. INTRODUCTION

WATER vapor, one of the most important components in the atmosphere, affects various atmospheric processes

Shangyi Liu, Kefei Zhang, Suqin Wu, Wenyuan Zhang, Longjiang Li, Moufeng Wan, Jiaqi Shi, and Minghao Zhang are with the School of Environment Science and Spatial Informatics, China University of Mining and Technology, Xuzhou 221116, China (e-mail: ts20160131p31@cumt.edu.cn; profkzhang@cumt.edu.cn; suqin_wu@cumt.edu.cn; zhangwy@cumt.edu.cn; lilongjiang@cumt.edu.cn; wanmoufeng@cumt.edu.cn; shijq@cumt.edu.cn; minghao_zhang@cumt.edu.cn).

Andong Hu is with the Cooperative Institute for Research in Environmental Sciences, Boulder, CO 80309 USA (e-mail: andong.hu@colorado.edu).

Digital Object Identifier 10.1109/JSTARS.2022.3192437

[1], [2]. Water vapor data with high accuracy and high temporal resolution play a vital role in weather forecasting, atmospheric modeling, disaster prevention and mitigation, and environment pollution monitoring [3]–[7]. Over the last two decades, global navigation satellite systems (GNSS) tropospheric tomography technique has gradually become a powerful technique for reconstructing three-dimensional (3-D) water vapor fields with both high spatial and temporal resolutions predominantly due to the advantages of low cost, high accuracy, and all-weather availability of the GNSS measurements. This technique was first realized by Flores [8] and Champollion *et al.* [9], and since then many studies and experiments on tropospheric tomography in various regions have been carried out [10]–[14]. However, unlike conventional computed tomography used in the medical field, for tropospheric tomography, GNSS data are often insufficient due to the sparse and uneven distribution of local continuously operating reference stations (CORS) networks and the limited number of GNSS satellites observed [15]. As a result, tropospheric tomography typically involves solving an ill-posed inverse problem, and tropospheric tomography modeling is still challenging for practical applications [16].

To solve the above mentioned ill-posed inverse problem, various tomographic methods have been proposed by scholars around the world, among which the algebraic iterative reconstruction (AIR) methods have been widely used [11], [17]–[19] for their advantages of avoiding complicated matrix inversion and saving computational cost. The two types of the AIR methods are sequential and simultaneous versions, namely algebraic reconstruction techniques (ARTs) [20] and simultaneous iterative reconstruction techniques (SIRTs) [21]. Some improved iterative algorithms have also been proposed for atmospheric tomography. For example, Wen [22] proposed an improved algebraic reconstruction technique (IART) and Yao [23] developed an adaptive simultaneous iterative reconstruction technique (ASIRT), in which the electron density of the voxels was introduced into the correction. Xia [24] presented a combined reconstruction algorithm, in which *a priori* water vapor information derived from COSMIC radio occultation (RO) data was employed as initial values of the IART. For the voxels that have no rays crossing, Gaussian filters [25], [26], Laplace operators [27], [28], and the inverse distance weighted (IDW) interpolation [29] methods were usually used to smooth the voxels. Some researchers applied the total variation method to reconstruct iterative regularized solutions with promising results [30], [31].

The projected iterative method is also effective for solving the ill-posed problem, in which additional constraints are added to the reconstruction in the classical AIR methods. Such constraints incorporate *a priori* knowledge of the solution, typically leading to a better tomographic result [32], [33]. Applications of the projected iterative methods in seismology, image restoration, electromagnetic tomography, and gravity fields can be found in [34]–[37]. In particular, the projected methods are used as nonnegativity constraints for the unknown parameters to be solved in the atmospheric tomography [31].

Although the feasibility of the above algorithms has been verified, the ill-posed problem of tropospheric tomography in the inversion process is a core issue and still requires further investigation. The performance of the iterative methods relies heavily on the selection of the initial values for the unknown parameters [25], [38], which are obtained mainly from empirical values or a numerical weather prediction model, e.g., the standard atmosphere [26], radiosonde (RS) data [10], [39], and global forecast products produced by National Centers for Environmental Prediction [11], [18], [40]. The accuracy of the empirical values is usually low due to the large spatiotemporal variation in water vapor distribution (as shown in Section V-C), and as a result, it often leads to uneven tomographic solutions. Some researchers also applied the results from noniterative methods as the initial values, e.g., from the least squares method [19] and COSMIC RO data [24]. However, the temporal resolution of the data other than GNSS is usually lower than GNSS data, which cannot support the real-time need for GNSS tropospheric tomography. Moreover, there are some difficulties for the least squares estimation in the determination of the weights of the observations and the determination of the inversion of the projection matrix which is time consuming. Another issue needing to be addressed is the selection of appropriate criteria for the termination of the iteration to ensure both computational efficiency and desired accuracy of the solution. The two main types of criteria used in previous articles include the back-projection technique, i.e., the iteration will be terminated when the reconstructed data are close to the observation data (meaning small residuals); if the difference between the fields of the unknown parameters over the current (e.g., kth) and previous ($k-1$th) iterations is below the predefined threshold, the procedure will be terminated [11], [24], [25], [30]. However, for the discrete ill-posed problem, small residuals from the back projection do not necessarily signify a good tomographic solution [41] (also shown in Fig. 1). The determination of the empirical thresholds is usually complicated with unstable solutions.

In this article, the inversion algorithm is examined to solve the above problems. First, the projected iterative methods based on ART, SIRT, and their improved versions—IART and ASIRT are realized. In these projected methods, it is assumed that the solution must belong to a convex set, and the hypothetical convex set is simulated by ERA5 data to constrain the voxels in each iteration. Then, a two-step projected iterative algorithm (TSPIA) that includes preprocessing for the initial values, which will be used as the input of the projected iterative method subsequently, is presented. In addition, the semi-convergence property of the iterative methods in tropospheric tomography is
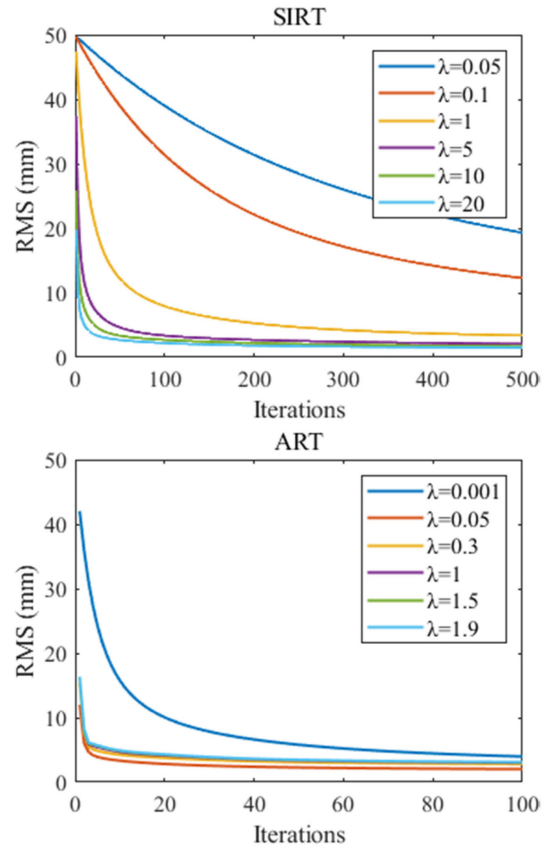

Fig. 1. Variation in the rms of the residual vector [see (19)] for (top) SIRT and (bottom) ART methods with the number of iterations and each selected constant λ value at 12:00 UTC, DOY 168, 2020 (same epoch as Fig. 2).

examined, and strategies for the determination of the relaxation parameters used in the (projected) ART and SIRT methods are provided. Moreover, a 2-D normalized cumulative periodogram (2-D-NCP) iterative termination criterion, which processes the observation signals in groups, is introduced for tropospheric tomography. To evaluate the feasibility and superiority of the proposed method, tomographic experiments using GNSS data from the Hong Kong CORS network during a wet and a dry periods were performed. The water vapor fields reconstructed from the new iterative methods and also some existing iterative methods for the comparisons of different methods are validated using RS profiles and ERA5 data as the two references.

II. PRINCIPLES OF TROPOSPHERIC TOMOGRAPHY

A. Tomographic Modeling

A GNSS signal transmitted from a GNSS satellite to a ground receiver is delayed due to the refraction of the neutral atmosphere. The tropospheric delay is commonly divided into two components: the hydrostatic delay caused by the neutral hydrostatic atmosphere and the wet delay due to the water vapor. Unlike the ionospheric delay, which can be well cancelled out from an ionospheric-free combination of simultaneous duel-frequency observations, the tropospheric delay needs to be estimated. In GPS data processing, the tropospheric delay along

the signal path is typically mapped to the zenith direction (zenith tropospheric delay, ZTD) of the station to reduce the number of the unknown parameters to be estimated, which avoids the rank deficiency of the observation equation system. The ZTD can be also divided into zenith hydrostatic delay (ZHD) and zenith wet delay (ZWD). The ZHD can be obtained from an empirical model, e.g., the Saastamoinen model [42], with a high accuracy. The ZWD can be calculated by subtracting the ZHD from the ZTD which is estimated from GNSS data processing

$$\text{ZWD} = \text{ZTD} - \text{ZHD}. \tag{1}$$

However, the ZWD, as the total value along the vertical direction, cannot reflect the vertical distribution of water vapor. To reconstruct the wet refractivity (WR) field from a tropospheric tomography, the ZWD needs to be mapped to the direction of the slant wet delay (SWD) along the signal ray path as the input observation of the tomography, which can be written as

$$\text{SWD} = m_w[\text{ZWD} + \cot\varepsilon(G_N\cos\varphi + G_E\sin\varphi)] + \delta \tag{2}$$

where m_w is the wet mapping function; G_N and G_E are the slant delay gradient parameters in the northern and eastern directions, respectively; ε and φ are the elevation angle and geographic latitude, respectively; and δ is the postfit phase residual.

By definition, SWD is the integral of the WR along the signal path [43]

$$\text{SWD} = 10^{-6}\int_s N_w ds \tag{3}$$

where N_w denotes the WR and s is the signal path from the satellite to the receiver. The geometric path delay caused by the bending of the ray is generally neglected and thus s is assumed to be a straight line [44].

Equation (3) can be resolved by discretizing the tomographic region into small 3-D voxels as

$$\text{SWD} \approx AX \tag{4}$$

where SWD, the observation vector of the tomography, is calculated by (2); A denotes the projection matrix, which is determined by the structure of the voxels and the length of the signals crossing through the voxels; and X is the unknown WR parameters vector of all the voxels. The WR in each voxel is assumed to be homogeneous and the WR value is fixed during the period of the tomography.

Equation (4) defines a large linear equations system with noise, which is ill-posed and overdetermined. Solutions of such a system are often nonunique and unstable, and small changes in the input values of the system may cause large perturbations in the solutions.

B. Classical Iterative Methods for Tomographic Inversion

As mentioned above, the AIR methods usually rely on matrix-vector multiplication. It avoids the inversion of a large projection matrix and saves computational cost, which is ideal for solving large-scale problems. In this section, the classical ART and SIRT methods, as well as their improved versions IART and ASIRT are examined.

The classical ART algorithm, also known as the Kaczmarz method [45], treats one observation signal at a time during the iterations. Its formula can be expressed as

$$x_j^{k+1} = x_j^k + \lambda_k a_{ij}\bigg/\sum_{j=1}^n a_{ij}^2\left(\text{SWD}_i - \sum_{j=1}^n a_{ij}x^k\right),$$
$$i = 1, 2, \ldots, m \tag{5}$$

where x_j^k denotes the WR value of the jth voxel in the kth iteration; n is the number of the columns of the observation equations, i.e., the number of the unknown parameters; a_{ij} is the element in the ith row and jth column of the coefficient matrix; m is the number of the observation equations; and λ_k is the relaxation parameter, which is usually a constant value and must satisfy $0 < \lambda_k < 2$. Based on ART, Wen [22] proposed the IART method, in which the correction factor $w_{ij}^k = \lambda_k a_{ij}/\sum_{j=1}^n a_{ij}^2$ in (5) is replaced with

$$w_{ij}^k = \lambda_k a_{ij}x_j^k\bigg/\sum_{j=1}^n a_{ij}^2 x_j^k. \tag{6}$$

In this method, the WR value estimated in the previous iteration is also taken into account in the correction factor.

The SIRT methods utilize all equations simultaneously in the correction factor to avoid the effect of the order of the observation equations on the solution. These "simultaneous" methods can be written in the general form as

$$x^{k+1} = x^k + \lambda_k DA^T M(\text{SWD} - Ax^k) \tag{7}$$

where $0 < \lambda_k < \rho(DA^T MA)$, $\rho(\cdot)$ is the spectral radius; while D and M are two symmetric positive definite matrices. In this article, the classical Cimmino method [46] in the SIRT group was selected, which can be expressed as

$$x_j^{k+1} = x_j^k + \frac{1}{m}\sum_{i=1}^m w_{ij}^k\left(\text{SWD}_i - \sum_{j=1}^n a_{ij}x^k\right). \tag{8}$$

If w_{ij}^k is the same as that in the ART formula expressed in (5), then (8) is for the SIRT method. Similarly, if w_{ij}^k is the same as that expressed in (6), then the equation is for ASIRT [23].

C. Inverse Distance Weighted (IDW) Interpolation

As mentioned previously, some voxels may not be crossed by any rays during the period of time of the tomography, mainly due to the sparseness of the ground GNSS stations and poor distribution of the GNSS satellites in view. The WR values in these voxels cannot be corrected by the iterative methods but remain the initial values. Therefore, we applied the IDW interpolation method to cope with this problem [29]. The general form of IDW is

$$x_0 = \sum_{i=1}^S \frac{x_i}{d_i}\bigg/\sum_{i=1}^S \frac{1}{d_i} \tag{9}$$

where x_0 is the WR value of the voxel interpolated for; x_i is the WR value of the voxel corrected by rays; d_i is the distance between the voxel interpolated for and the voxel corrected by

Method	Type	Correction factor	Projection
ART	sequential	$w_{ij}^k = \lambda_k\, a_{ij} \Big/ \sum_{j=1}^n a_{ij}^2$	No
IART	sequential	$w_{ij}^k = \lambda_k\, a_{ij} x_j^k \Big/ \sum_{j=1}^n a_{ij}^2 x_j^k$	No
P-ART	sequential	$w_{ij}^k = \lambda_k\, a_{ij} \Big/ \sum_{j=1}^n a_{ij}^2$	Yes
P-IART	sequential	$w_{ij}^k = \lambda_k\, a_{ij} x_j^k \Big/ \sum_{j=1}^n a_{ij}^2 x_j^k$	Yes
SIRT	simultaneous	$w_{ij}^k = \lambda_k\, a_{ij} \Big/ \sum_{j=1}^n a_{ij}^2$	No
ASIRT	simultaneous	$w_{ij}^k = \lambda_k\, a_{ij} x_j^k \Big/ \sum_{j=1}^n a_{ij}^2 x_j^k$	No
P-SIRT	simultaneous	$w_{ij}^k = \lambda_k\, a_{ij} \Big/ \sum_{j=1}^n a_{ij}^2$	Yes
P-ASIRT	simultaneous	$w_{ij}^k = \lambda_k\, a_{ij} x_j^k \Big/ \sum_{j=1}^n a_{ij}^2 x_j^k$	Yes

nearby passing through rays; and S is the total number of the voxels corrected by rays.

III. IMPROVED ITERATIVE METHODS FOR TOMOGRAPHIC INVERSION

A. Projected Iterative Methods

In this section, the projected versions of the aforementioned iterative methods are presented. Let C be a closed convex set and P_C be an orthogonal projection on C, then the box constraint [48] expressed by C for each voxel is

$$C = [l_1, u_1] \times [l_2, u_2] \times \cdots \times [l_j, u_j] \times \cdots [l_n, u_n] \quad (10)$$

where l_j and u_j represent the lower and upper bounds of the jth voxel, respectively. The box constraints work in each time of the iteration for the projected methods and work in each observation signal, especially for P-ART. When the WR estimates of the voxels are beyond the constraints scope, they are corrected using

$$x_j^{k\,(P)} = \begin{cases} l_j, x_j^k < l_j \\ u_j, x_j^k > u_j. \end{cases} \quad (11)$$

Therefore, the algorithms of P-ART and P-SIRT can be expressed as

$$x_j^{k+1} \leftarrow P_C\left(x_j^k + \lambda_k \frac{a_{ij}(\mathrm{SWD}_i - \sum_{j=1}^n a_{ij} x^k)}{\sum_{j=1}^n a_{ij}^2} \right) \quad (12)$$

$$x_j^{k+1} \leftarrow P_C\left(x_j^k + \frac{1}{m}\lambda_k \sum_{i=1}^m \frac{a_{ij}(\mathrm{SWD}_i - \sum_{j=1}^n a_{ij} x^k)}{\sum_{j=1}^n a_{ij}^2} \right). \quad (13)$$

Furthermore, the P-IART and P-ASIRT algorithms can be obtained according to IART and ASIRT, respectively. All these iterative regularization methods are listed in Table I.

In this article, the upper and lower bounds of the box constraints were determined according to the *a priori* information of the water vapor, and if the tomographic solutions were beyond the bounds, they were considered as abnormal. Due to some

degrees of temporal and spatial regularities in the water vapor variation, it was assumed that the WR values within the same voxel in the same month but in different years obey a normal distribution. Therefore, the hypothetical convex set expressed by (10) can be simulated based on the historical WR data from hourly ERA5 during the month the same as the tomographic month but in the previous year. To obtain the ERA5 WR at each tomographic voxel, the IDW interpolation was applied for the vertical direction (i.e., the voxels in the same vertical column) and the bilinear interpolation was applied for the horizontal domain (i.e., the voxels in the same height layer). The upper and lower bounds for the jth voxel can be expressed as

$$\begin{cases} l_j = \mathrm{mean}_j - 3\mathrm{std}_j \\ u_j = \mathrm{mean}_j + 3\mathrm{std}_j \end{cases} \quad (14)$$

where mean_j and std_j are the mean and standard deviation (STD) of the WR values of the month in the jth voxel, respectively. In addition, due to the nonnegative nature of WR, nonnegativity constraints were also added into the box constraints

$$l_j = \begin{cases} l_j, l_j \geq 0 \\ 0, l_j < 0. \end{cases} \quad (15)$$

B. TSPIA

In this section, the TSPIA, which was based on the box constraints expressed by a convex set, is elaborated. First, the preprocessing for determining the initial values of the WR fields is performed. These values are cyclically adjusted, according to the convex set and the observations; then its result is input into the projected iterative method and iteratively improved.

In the first step of the preprocessing, to quantitatively evaluate the availability of the initial values, two parameters Cn and Ch are defined in the inversion, where P-ART with one iteration is used as the inversion method. Cn denotes the ratio of the number of box-constrained corrections to the number of the observations, while the vector Ch is the number of box-constrained corrections at each layer. It should be noted that, if the input initial values are relatively close to their truth values, then the solution is hardly be corrected by the box constraints. Moreover, more attention needs to be paid to anomalous solutions near the ground layers rather than high-altitude voxels in the inversion, since in high-altitude layers the difference between the upper and lower bounds of the box constraints is relatively small, but the correction in ART determined by the intercepts of the signals is large. Thus, some corrections in the high-altitude grids do not imply that the initial values are poor.

The preprocessing for the initial values consists of two loops, an inner loop and an outer loop, which are similar to ART. The inner loop is for processing all the voxels at each height layer and the outer loop is for all integrations. Within the inner loop, all the voxels at the current height layer are processed in one go, and different schemes for the initial values are input into P-ART. The scheme that results in the smallest is considered optimal, and thus to be incorporated into the next layer. When the processing for all height layers is completed, the outer loop starts the next iteration. More details for this process are as follows.

1) Initialize the following parameters: the time of the maximum iteration $k_{n\max}$ and the number of the iterations k_n in the outer loop; the iterative step delta in the inner loop; the iterative relaxation factor ω for P-ART; and the initial value vector $X0$, which is assigned to the mean of the historical RS data within the 3-day time window before the tomographic epoch.
2) Inner loop processing.
   a) Calculate two sets of initial values $X1$ and $X2$ for each voxel based on $X0$. For example, if the current processing is for the kth layer, then assign all the voxels of this layer to $X1_i = X0_i -$ delta, $X2_i = X0_i +$ delta; while for all voxels in the other layers, assign $X1_i = X0_i$ and $X2_i = X0_i$, where i denotes the index of the voxel.
   b) Input different schemes ($X0$, $X1$, and $X2$) into the P-ART algorithm as the initial values with one iteration and calculate their corresponding Cn and Ch.
   c) Select the optimal scheme from different schemes by comparing their resultant Cn values; then the result from the optimal scheme is used as the new initial value vector $X0$ to be incorporated into the next layer.

Repeat the above steps a)–c) until all the layers are processed. Then, output the current $X0$ and assign the number of the outer loop iteration $k_n = k_n + 1$. For the tests carried out in this article, the related parameter assignments were $k_{n\max} = 30$; $\omega = 0.05$; and delta$= 0.5$ if the layer numbering ≥ 7, otherwise delta$= 1$.

3) Determine the termination criteria for the iterations. The iteration will terminate if either the processed $X0$ is as desired or the predefined value for the number of the iterations is satisfied. In this article, when correction made by box constraints takes place only in the top grids and the times of the corrections are sufficiently small (e.g., $Cn <$ 0.05 was adopted in this article), the initial value would be regarded fine. In addition, the order of the height layers in the inner loop is taken as following: Initially, we set the inner loop order from low to high layers ($k = 1, 2 \cdots$ 10), and if the output $X0$ from three consecutive iterations were stable, then we randomly set the order of the height layers in the inner loop.

Next, the solution resulting from step 1) will be used as the input of the projected iterative methods, and different projected iterative algorithms lead to different forms of TSPIA. These will be discussed in the following sections.

C. Semi-Convergence of Iterative Methods

When the data used for tomography are noisy, which is not uncommon, the semi-convergence properties of the iterative methods need to be considered. The accuracy of the solution improves first but then becomes degraded during the iteration process, instead of showing instead of asymptotic convergence. The studies on the semi-convergence theory of the iterative methods and their projected versions can be found in [33], [47]–[49].

In this section, the semi-convergence mechanism of the iterative methods for the water vapor tomography system $SWD \approx AX$ is analyzed with the notations defined as

$$\text{SWD} = \bar{b} + R, \quad R = \text{residual}, \quad \bar{b} = A\bar{x} = \text{dummy vector},$$
$$\bar{x} = \text{exact solution}, \quad \overline{\text{SWD}} = \text{exact SWD}. \tag{16}$$

R is the essential factor of the semi-convergence behavior, which can be explained by two components R_1 and R_2 as follows:

$$R = \text{SWD} - \bar{b} = \text{SWD} - A\bar{x}$$
$$= (\text{SWD} - \overline{\text{SWD}}) + (\overline{\text{SWD}} - A\bar{x})$$
$$= R_1 + R_2. \tag{17}$$

R_1 represents the uncertainty of the SWD estimated from GNSS data, which mainly includes the uncertainty of the ZTD and the satellite's elevation [50]. While R_2 is mainly composed of the discretization error and the error from the assumption that the signal path is a straight line in (4).

To further illustrate the semi-convergence mechanism, the reconstructed difference $\bar{x} - x^k$ in the kth iteration is divided into two parts [47]

$$\bar{x} - x^k = (\bar{x} - \bar{x}^k) + (\bar{x}^k - x^k) \tag{18}$$

where the iteration vector $\bar{x}^k$ corresponds to the R-free dummy vector $\bar{b} = A\bar{x}$. First part denotes the iteration error, which gradually decreases with iteration and is similar to asymptotic convergence theory. Second part represents the noise error, which is due to the presence of R and tends to increase with iteration. Whether the semi-convergence is apparent depends on how fast this part increases. Fig. 2 shows the variation in the root mean square error (RMSE) of different iterative methods applied in water vapor tomography with the number of iterations. These numerical examples clearly demonstrate semi-convergence behaviors. Moreover, as shown in Fig. 3, when the input value of the tomographic system is the dummy vector $\bar{b}$, the method exhibits asymptotic converge with iteration, where $\bar{x}$ was simulated based on ERA5 data. In addition, different iterative methods and different relaxation parameters lead to different semi-convergence behaviors. As we can see, ART reaches the optimal point in a fewer iterations compared with SIRT, and the larger the relaxation parameter, the more obvious the semi-convergence.

IV. CONFIGURATION FOR TOMOGRAPHIC SYSTEM

A. Tomographic Configuration and GPS Data Processing

As shown in Fig. 4, observations from the CORS network consisting of 12 GNSS stations equipped with Leica receivers and antennas in Hong Kong were selected for the tomographic experiments in this article. All these stations were equipped with an automatic meteorological device for measuring temperature, air pressure, and relative humidity. The average distance between these stations is about 10 km and their altitude is within 350 m, indicating flat terrain. The selected study area is roughly within the range of $113.87° - 114.35°$E, $22.19° - 22.54°$N, and
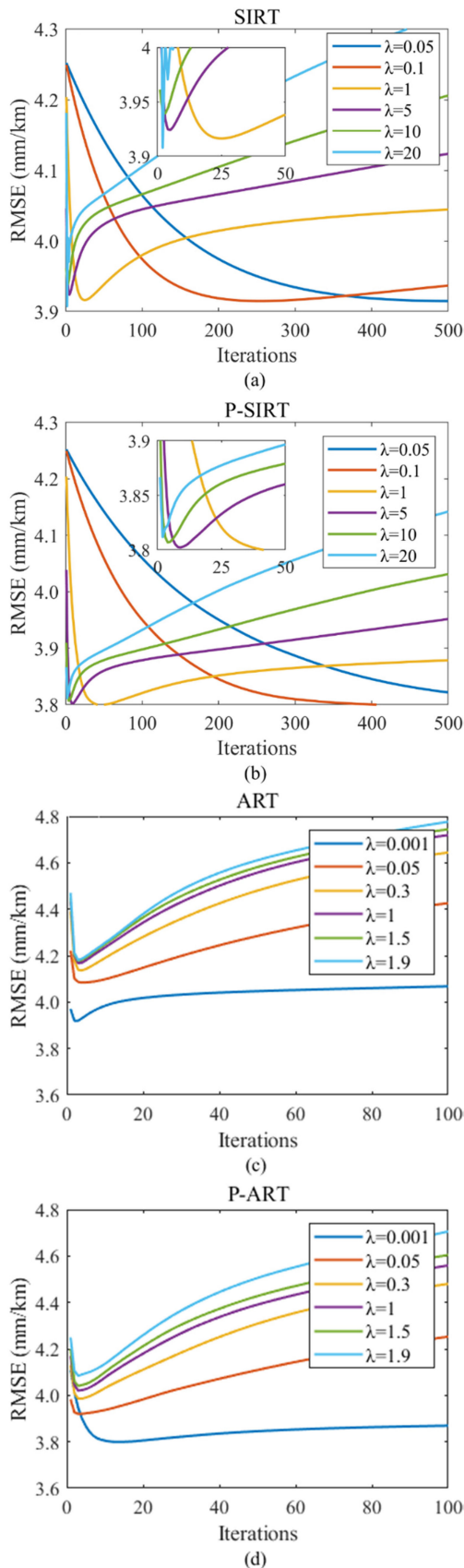
Fig. 2. Variation in the RMSE of the (projected) AIR methods with the number of iterations and each selected constant λ value at 12:00 UTC, DOY 168, 2020. (a) SIRT. (b) P-SIRT. (c) ART. (d) P-ART.

$0-10$ km in the longitudinal, latitudinal, and vertical directions, respectively. In this article, a 0.5 h temporal resolution was adopted for the tomographic modeling. The division for the voxels of the tomographic region is as follows. The origin coordinates of the unified station-origin coordinate system were defined as: B $=$ 22.40°, L $=$ 114.11°, and H $=$ 0 km. In the horizontal domain, there were six voxels with each covering approximately 8.25 km in the east–west direction and five voxels with each covering approximately 7.75 km in the north–south direction. In the vertical direction, 10 layers were determined with the following step from the bottom to the top: 0.6, 0.6, 0.8, 0.8, 1.0, 1.0, 1.0, 0.9, 1.2, 1.4, and 1.6 km, according to the general principle that WR decreases with height.

In this article, the Bernese 5.2 software with the precise point positioning technique [51] was used to estimate hourly ZTDs and horizontal gradients from GNSS data, and the global mapping function projection function was adopted [52]. The ZHD was obtained using the Saastmaoinen model, for which pressure data from ERA5 were used. The SWD was calculated from (1) and (2).

Two periods of GNSS data were processed for the tropospheric tomography. One is the wet period from DOY 153 to 182, 2020, with the total rainfall of 397.2 mm; and the other is the dry period from DOY 335 to 365, 2019, with the total rainfall of only 13.5 mm. The statistics can be found.[1]

B. Strategies for Selection of Relaxation Parameter

The function of the relaxation parameter λ is twofold, which is to ensure global convergence and fast convergence by varying its magnitude and to restrain errors related to semi-convergence [33]. In this section, the strategies for the selection of the relaxation parameter for the (projected) SIRT and the (projected) ART methods are provided.

For the (projected) SIRT methods, their optimal accuracy is almost independent on λ (except in the case that it is close to the maximum allowed), which can be seen in Fig. 2(a) and (b). This means that a large but not too close to the maximum allowed value can be selected for λ to improve computational efficiency. The "ψ_2-strategy" [33], a step-size decreasing strategy, was used in this article for controlling the noise error.

For the (projected) ART methods, the relationship between λ and the solution accuracy is much more complicated. First, for the classical ART method, the smaller the λ value, the better the optimal accuracy, as shown in Fig. 5(a). However, a too small λ value is likely to cause slow convergence; thus, a balance between the accuracy and efficiency of the solution needs to be considered. It is recommended that a small but not too small constant value for λ (e.g., $\lambda = 0.05$ was adopted in this article) for the classical ART method. However, this rule may be changed for some epochs for the P-ART method, where a larger λ value is likely to result in a better solution, as shown in Fig. 5(b). This is because the added constraints can restrain the accumulation of the errors in the tomographic solution during the iterations, particularly for a large λ value. Another reason for the change
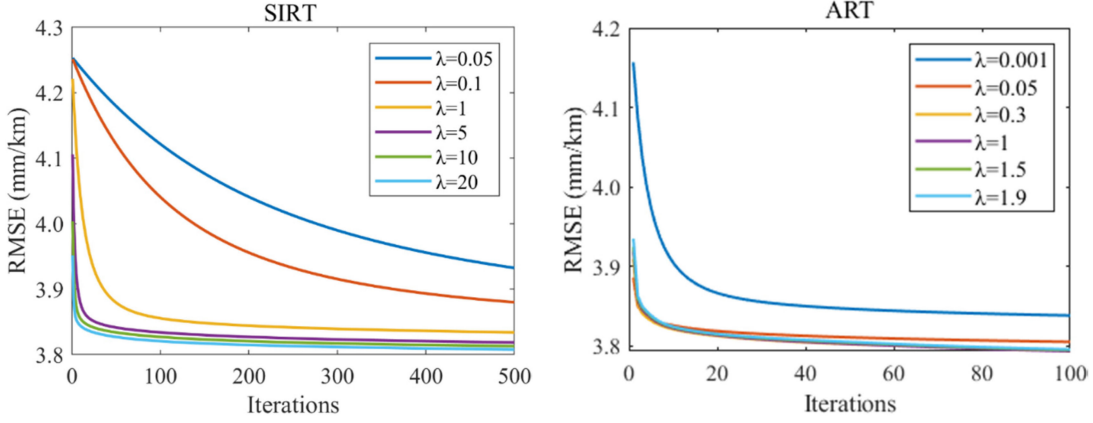
Fig. 3. Variation in the RMSE of the (left) SIRT and (right) ART methods with the number of iterations at 12:00 UTC, DOY 168, 2020 (same epoch as Fig. 2) where the residual R [see (16)] is removed from the input value of the tomographic system.
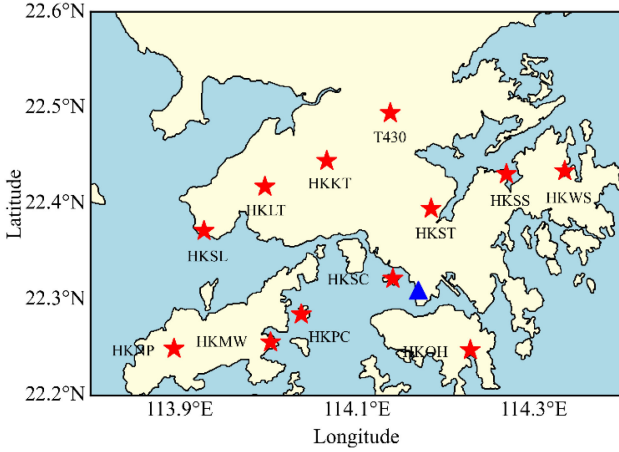

Fig. 4. Tomographic area covered by 12 GNSS CORS stations (red stars) and the radiosonde station (blue triangle) in Hong Kong.

of the rule is related to the structure of the initial values for the unknown parameters. Fig. 5(c) shows the variation in the RMSE of the projected ART with the number of iterations after the initial values obtained from preprocessing were applied, which is similar to the classical ART method.

For the constrained case, we still recommend to adopt a small constant value for λ (e.g., λ = 0.05) for maintaining the stability of the solution because it is difficult to forecast the aforementioned special situation, which can be seen in Fig. 5(b), and this special situation may change after the initial values from preprocessing are applied.

C. Termination Criteria for Iteration

There are none of universal standards for the termination criteria of an iteration used in the AIR methods. For a reasonable criterion, both computational efficiency and solution accuracy need to be taken into account. As mentioned above, in previous articles, the back-projection technique is commonly used as the termination criterion. Some statistical parameters for the residual vector $r_k = \text{SWD} - \langle A, x^k \rangle$, e.g., the average value (AVE) and rms, are often used to indicate the convergence

behavior and the accuracy of the reconstruction [11], [24], [25], [40]. Their formulas are

$$
\begin{cases}
\text{AVE} = \frac{1}{m} \sum_{i=1}^{m} \left(\text{SWD}_i - \langle A_i, x^k \rangle \right) \\
\text{RMS} = \sqrt{\frac{1}{m-1} \sum_{i=1}^{m} \left[\left(\text{SWD}_i - \langle A_i, x^k \rangle \right)^2 \right]}
\end{cases} . \tag{19}
$$

The iteration can be terminated if the back projection $\langle A_i, x^k \rangle$ is close to the observation data, i.e., the rms or AVE is smaller than the preset threshold. Another way is to compare the state vector x^k between consecutive iterations—if the difference of the unknown parameters between several consecutive iterations is under the preset threshold, then the iterative procedure is terminated.

However, for the discrete ill-posed problems, a small residual does not signify a good solution due to the semi-convergence property [41]. It can be seen in Figs. 1 and 2(a) and (c) that the residual does not accurately reflect the variation in the accuracy of the solution. The rms of the SIRT and ART residuals gradually decreases and remains stable with the number of iterations, while the accuracy of the two methods enhances first but then deteriorates during the iterations. Moreover, it is not easy to select a reasonable empirical threshold as its performance may be unstable.

The semi-convergence of the iterative methods used to determine the termination criteria also needs to be considered. Many rules for the selection of parameters for inverse problems can be used as the termination rules for the AIR methods. For example, the NCP criterion [53], [54], which treats the residual vector as a time series, and when it is sufficiently close to white noise, then the iteration can be terminated. Although the NCP rule has been applied in water vapor tomography by He *et al.* [55], it may be still problematic. For the system $SWD \approx AX$, if the solution is close to the truth, r_k will be close to R [see (16)], rather than white noise. From the analysis in Section III-C, different ground stations and different elevation angles result in different R values. Fig. 6 shows the relationship between the mean of the R values from different elevation angles and different ground stations at a single epoch. Fig. 7 shows the scatter diagram of the R values over the wet period studied. Clear distinction can be observed in the positive and negative property and magnitude
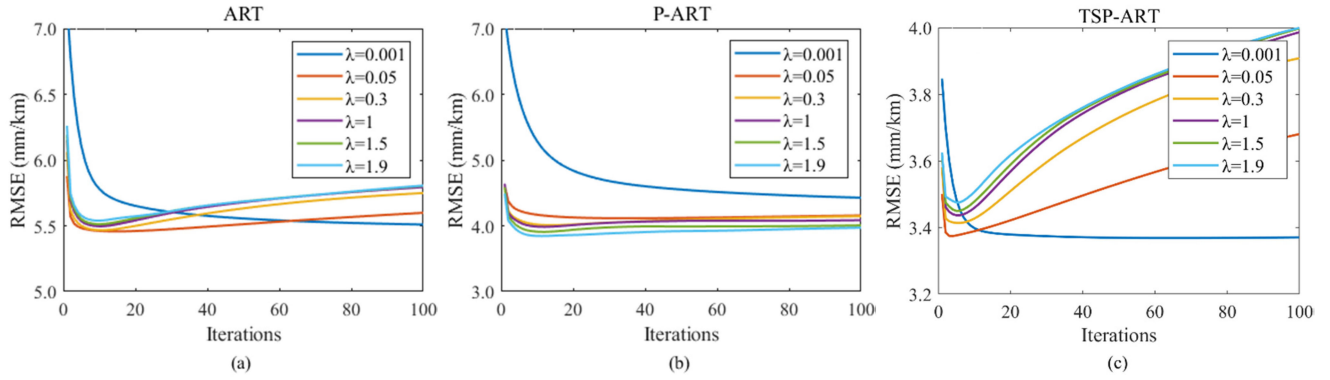
Fig. 5.   Variation in the RMSE of three ART algorithms with the number of iterations and each selected constant λ value at 12:00 UTC, DOY 154, 2020. (a) ART. (b) P-ART. (c) TSP-ART.
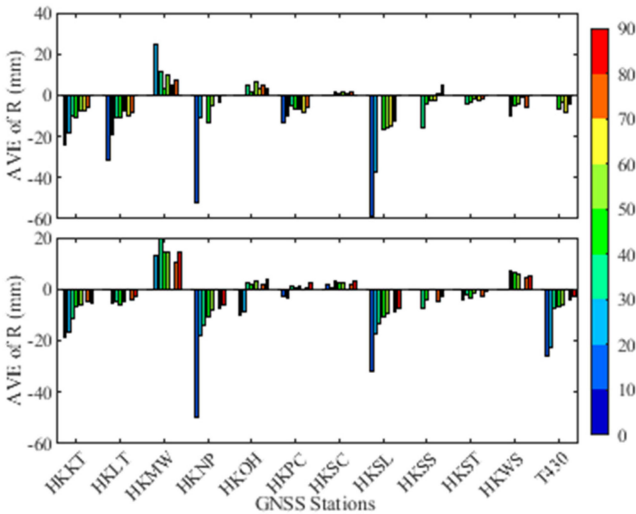

Fig. 6.   AVE of R values resulting from different elevation angles at each GNSS station at different time epochs. (Top) 12:00 UTC, DOY 154, 2020. (Bottom) 0:00 UTC, DOY 169, 2020.
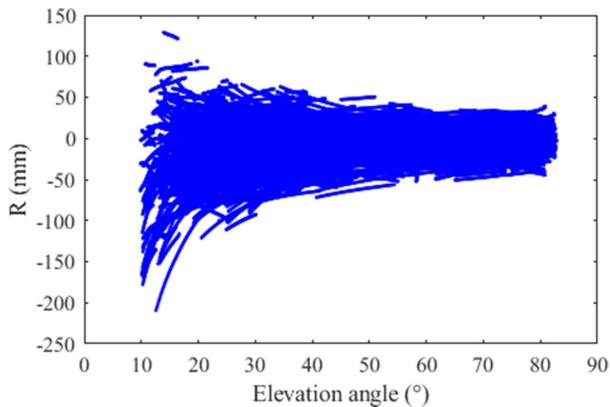

Fig. 7.   Scatter diagram of R values with elevation angles at 00:00 and 12:00 UTC on each day of the wet period.

between the R values of different stations, and at the same station the R value decreases with the increase in the elevation angle.

According to the software package in [47], a 2-D-NCP termination rule for tropospheric tomography is proposed. In this rule, the SWD and r_k vectors are reorganized into p subvectors [see (20) below], depending on the source of the signals, due to the correlation between the R value and the ground GNSS station:

$$\text{SWD} = \begin{pmatrix} \text{SWD}_1 \\ \text{SWD}_2 \\ \vdots \\ \text{SWD}_P \end{pmatrix}, \quad r^k = \begin{pmatrix} r_1^k \\ r_2^k \\ \vdots \\ r_p^k \end{pmatrix} \quad (20)$$

where p denotes the number of all subvectors, and each subvector corresponds to a single projection. Moreover, in this article, the rays with elevation angles less than 30° were excluded from the use in the determination of the iteration termination, due to their large R values and low accuracy. Then, the mean of the deviation of each subvector from white noise was calculated to measure the deviation of rk, and when the mean of the deviations reaches the minimum point the iteration will be terminated. More details are referred to [47].

V. RESULTS AND DISCUSSION

Since the RS data in Hong Kong, used as a reference of GNSS tropospheric tomography, are only available at 0:00 and 12:00 UTC daily, tomographic results only at these two epochs can be validated. Moreover, the RS data also need to be interpolated for those tomographic nodes for the validation [13]. The WR obtained from ERA5 data was also used as the other reference of the tomographic results of this article.

In this section, test results for the availability of the hypothetical convex set during the tomographic periods studied are presented first, then the accuracy and efficiency of the 2-D-NCP rule with the conventional rules for the termination of iteration are compared, followed by analyses for the stability and superiority of the algorithm proposed in this article in comparison with the conventional methods. The experiment with additional simulated observation errors further demonstrates the advantages of the proposed algorithm.

	Wet period			Dry period		
	Rate	AVE	RMS	Rate	AVE	RMS
RS	1%	−7.84	8.05	3.16%	−4.08	5.04
ERA5	0.26%	−2.45	2.79	3.06%	−5.09	6.23

A. Evaluation of Box Constraints

The box constraints were simulated based on historical ERA5 data. They define the upper and lower bounds of each voxel and may not agree well with the true WR field at some tomographic epochs. The error in the box constraints can be calculated as follows:

$$E_j = \begin{cases} \overline{x_j} - l_j, \overline{x_j} < l_j \\ u_j - \overline{x_j}, \overline{x_j} > u_j \end{cases} \quad (21)$$

where E_j and $\overline{x_j}$ are the error and reference of the jth voxel, respectively. Statistical results of the box constraints over the wet and dry periods studied are shown in Table II. The error rate is only about 3% even over the dry period when water vapor varied drastically and the vertical distribution is very uneven, meaning that the box-constrained method is feasible.

B. Validation of 2-D-NCP Termination Rule

The ART and SIRT methods and their projected versions were tested using data during the wet period studied to illustrate the advantages of using the termination rule from the 2-D-NCP. To visualize the performances of the termination criteria, the ratio of the number of the iterations determined by the termination criteria to the number of the iterations that results in the best accuracy ($K_{\text{rule}}/K_{\text{opt}}$), and its corresponding RMSE ratio ($\text{RMSE}_{\text{rule}}/\text{RMSE}_{\text{opt}}$) were calculated, for which ERA5 data were selected as the reference. Ideally, both ratios are close to 1. If $K_{\text{rule}}/K_{\text{opt}} < 1$, the termination is too early, otherwise too late. Furthermore, if the $\text{RMSE}_{\text{rule}}/\text{RMSE}_{\text{opt}}$ is too large, then the termination criterion is not well effective. As seen in Fig. 8, most of the data points are located within the interval $0 < K_{\text{rule}}/K_{\text{opt}} < 1$, indicating that the 2-D-NCP criterion does not have the risk of taking too many iterations.

For the (projected) ART method, the termination criterion given by Xia [24] called TRA was also selected for a comparison, and the maximum iterative number was set to 200. The TRA rule defines that the iteration terminates when the difference of the RMSs [see (19)] between the kth and $k+1$th iterations is under 0.001 mm. As we can see in Fig. 9(a) and (b), the advantages of the accuracy and computational efficiency of 2-D-NCP are noticeable, and 2-D-NCP also avoids complex work on the selection of empirical thresholds.

For the (projected) SIRT method, the termination criterion given by Zhang et al. [39], which is named TRA2 here, was selected for a comparison. Based on TRA2, the iteration will terminate when the STD of the rmss in five consecutive iterations is under 0.0016 mm, or the times of the iterations reaches 1000. Fig. 9(c) and (d) shows the comparison of the performances of
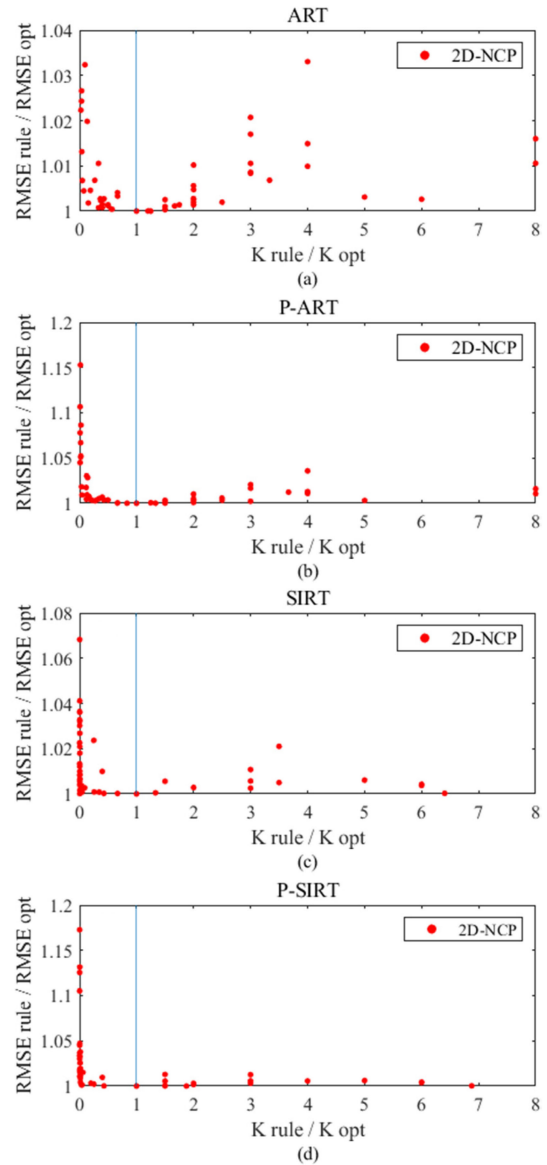

Fig. 8. Performances of the 2-D-NCP criterion for ART and SIRT, and their projected versions during the wet period. (a) ART. (b) P-ART. (c) SIRT. (d) P-SIRT.

the two criteria defined by TRA2 and 2-D-NCP. It can be seen that the 2-D-NCP criterion leads to a slightly lower accuracy but a much better computational efficiency. This suggests that it is more suitable for a near real-time mode.

C. Validation and Analysis of TSPIA

Experiments for performance evaluations of different AIR methods were carried out for the evaluation of the stability and superiority of TSPIA. The related parameters were set as follows. The maximum times of iterations was set to 500 with $\lambda = \psi_2$—strategy for the SIRT methods. The maximum times of iterations was set to 200 with $\lambda = 0.05$ for the ART methods. Moreover, the 2-D-NCP termination criterion was used for all scenarios. It is noted that the ASIRT algorithm with $\lambda = \psi_2$—strategy did not converge at some epochs during the dry
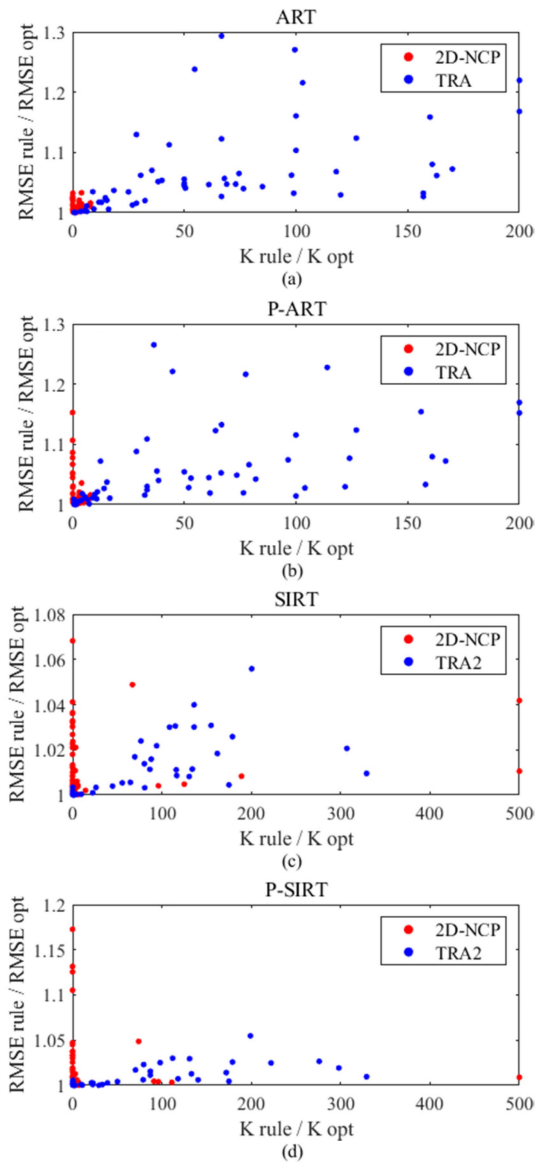
Fig. 9. Comparison of the performances of 2-D-NCP and traditional rules for ART and SIRT, and their projected versions over the wet period. (a) ART. (b) PART. (c) SIRT. (d) P-SIRT.

period studied. Instead, a 0.5 step size and the data range $0 < \lambda < 10$ were set to search the optimal relaxation parameter value. The λ value that led to the minimum RMSE during the dry period studied was selected for ASIRT.

Fig. 10 illustrates water vapor vertical profiles derived from different algorithms and RS on rainy and rainless days during the wet and dry periods, respectively. The water vapor profiles represent the WR values along the column of the voxels that is colocated with the RS station. It should be noted that only the results of the ART methods are shown in the figure because the tomographic results from the two types of AIR methods are similar. It can be seen that the WR profiles obtained by the proposed algorithms agree well with the RS profiles and better than that of the conventional algorithms on the both rainy and rainless days selected.

To quantitatively compare the WR retrievals of different tomographic methods, the mean of the RMSEs of WR from different algorithms for each epoch were calculated (Fig. 11), and RS data were used as the reference although the data at some epochs missed. The figure shows that the tomographic results from TSPIA are more accurate than that of the conventional methods at almost all epochs. Moreover, the TSPIA can correct those abnormal results effectively, compared with the traditional algorithms, and maintain good stability, as shown in Fig. 11. Statistical parameters including RMSE, mean absolute error (MAE), and bias of the tomographic results are listed in Table III. One can see that the mean RMSE of ART during the wet and dry periods are 7.52 and 9.22 mm/km, respectively, while that of the TSP-ART are 6.79 and 8.01 mm/km, with accuracy improvements of 9.71% and 13.12%. And the mean RMSE over the two periods reduces from 8.34 and 8.71 mm/km of IART to 7.30 and 7.83 mm/km of TSP-IART, which is equivalent to the improvement rates of 12.47% and 10.10%, respectively.

Besides, the mean of the RMSEs at all altitudes over the RS station during each of the two periods is shown in Fig. 12. It is noticed that although the performance of IART well improves at high altitudes in comparison with ART, which updates corrections according to the WR obtained from the previous iteration, it may also magnify the effect of the errors in the solution at low layers. In contrast, the proposed TSPIA has a better accuracy and better stability at almost all layers. Moreover, in the tomographic layers from 0 to 2 km, the RMSE evidently reduces from 12.43 mm/km of IART to 10.40 mm/km of TSP-IART; and the improvement in the vertical range from 7 to 10 km is significant with the mean of the RMSEs from 5.18 mm/km of ART to 2.38 mm/km of TSP-ART during the wet period.

Additionally, it is noticeable that the accuracy of the wet period is always significantly better than that of the dry period. Compared with the dry period, the RMSEs of TSP-ART and ART during the wet period decrease by 1.22 and 1.7 mm/km, respectively. This may be because the vertical distribution of water vapor during a wet period is more even and the spatiotemporal variation is more stable than that of a dry period. The tomographic results will be adversely affected if there are fluctuations in water vapor distribution with time and space [13], [56]. Furthermore, the water vapor distribution during the dry period does not show an exponential decrease with height at some epochs and even possibly has an inverse increase trend near the surface, as shown in Figs. 10 and 13.

More drastic temporal and spatial variations of water vapor make the effect of empirical initial values of the WR fields on the tomographic solutions more unstable. Therefore, the TSPIA is advantageous during the dry period since it uses the initial values obtained from preprocessing rather than empirical values.

To better visualize the 3-D water vapor distribution improved by the proposed method, the RMSE of each voxel over each of the wet and dry periods from different algorithms is shown in Fig. 14, and ERA5 data were used as the reference. We can see that the results of TSPIA agree better with the WR fields from ERA5 data than that of the conventional algorithms, and the abnormal solutions that are from the conventional algorithms are effectively improved by TSPIA.
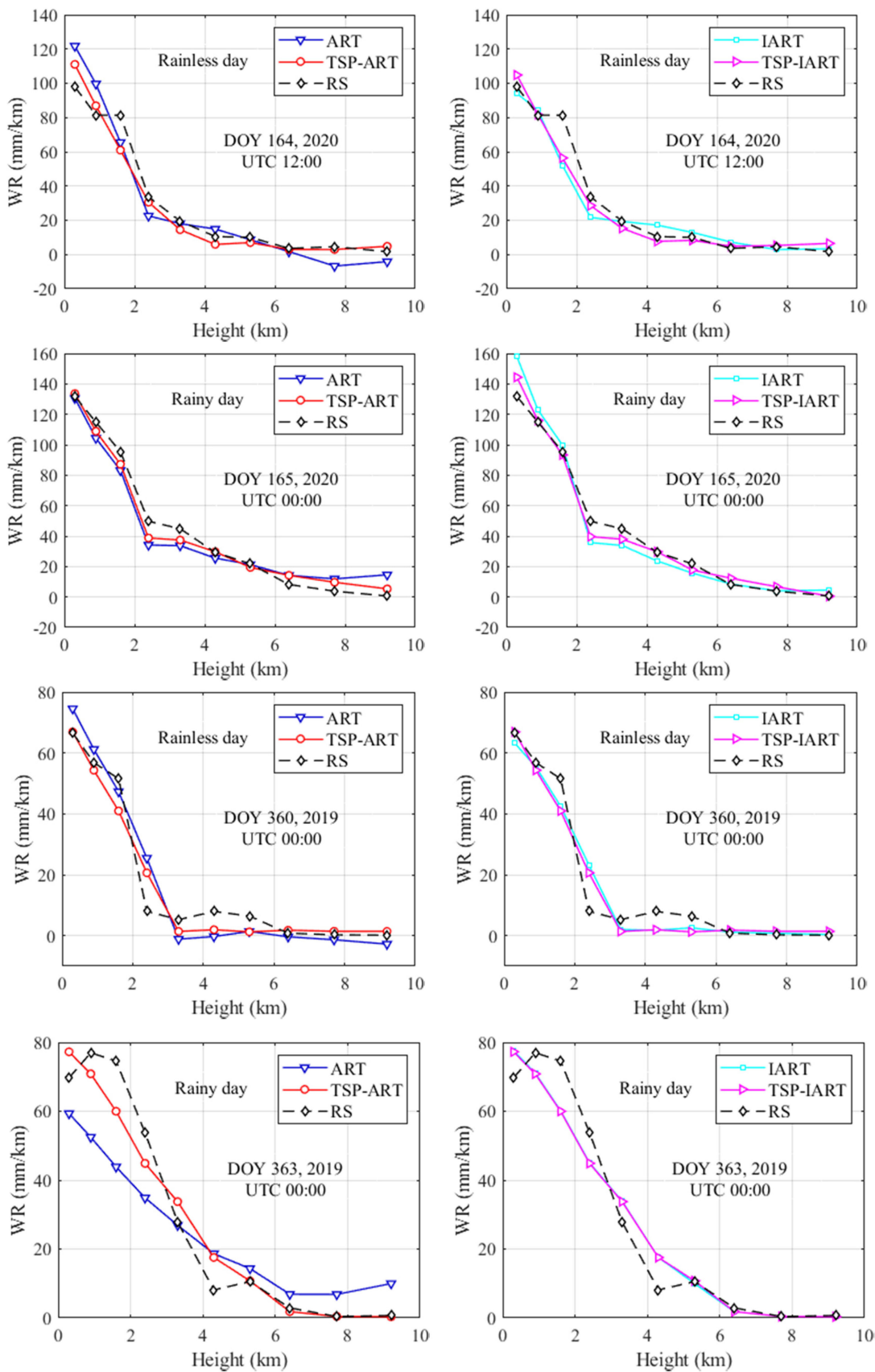
Fig. 10. Comparison of the water vapor profiles retrieved from TSPIA, conventional methods, and radiosonde data for rainless and rainy days over the two periods studied.
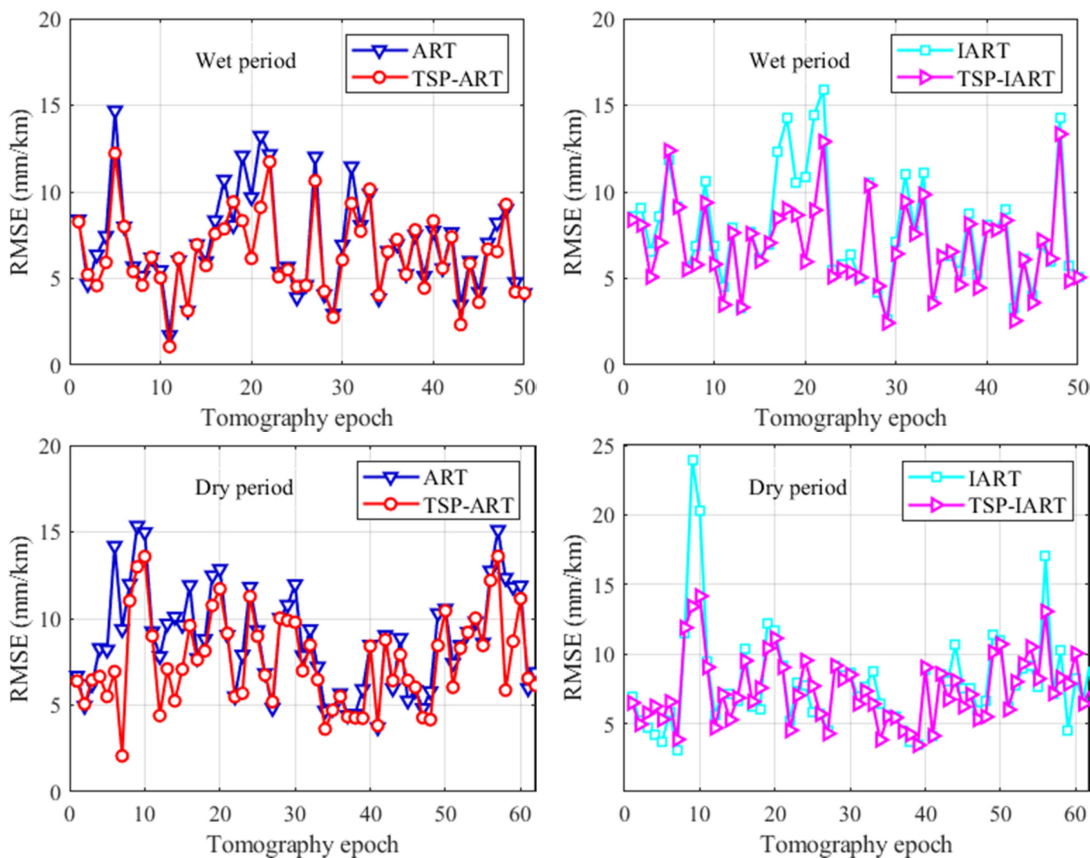
Fig. 11.   Comparison of the RMSE of the tomographic results resulting from different algorithms during the (top) wet and the (bottom) dry periods.
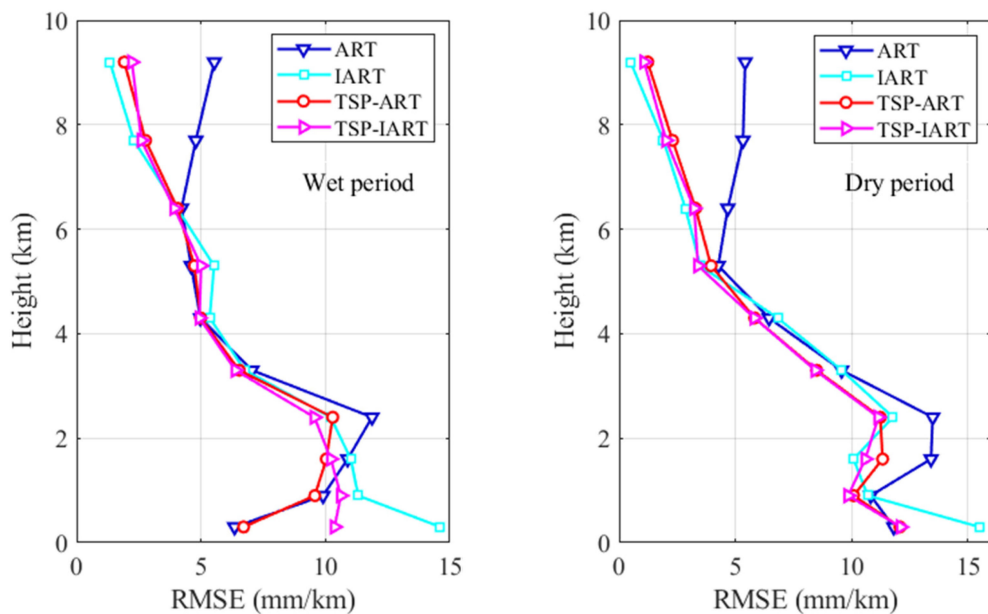

Fig. 12.   Mean of the RMSEs of the voxels at the same height resulting from four algorithms over the (left) wet and the (right) dry periods (radiosonde data were used as the reference).
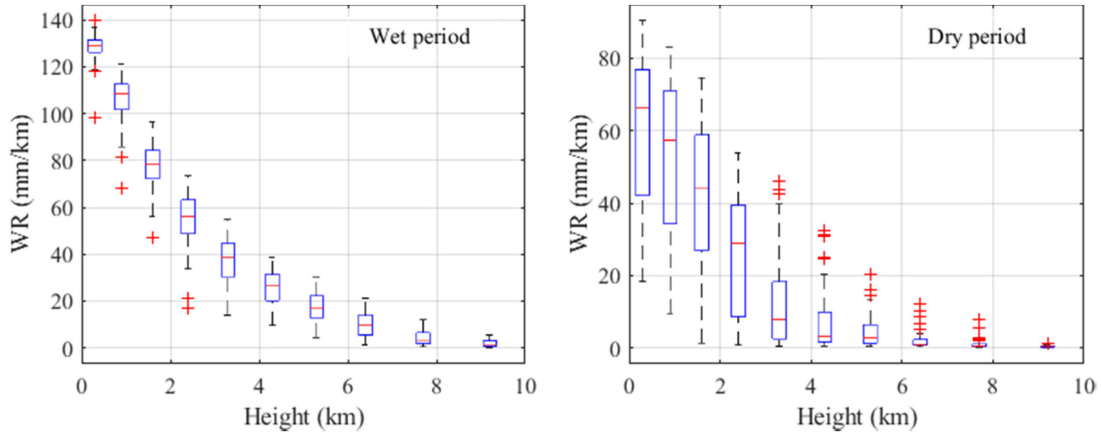
Fig. 13. Box plots of the WR values from radiosonde along the altitude of a column of voxels over the (left) wet and the (right) dry periods.
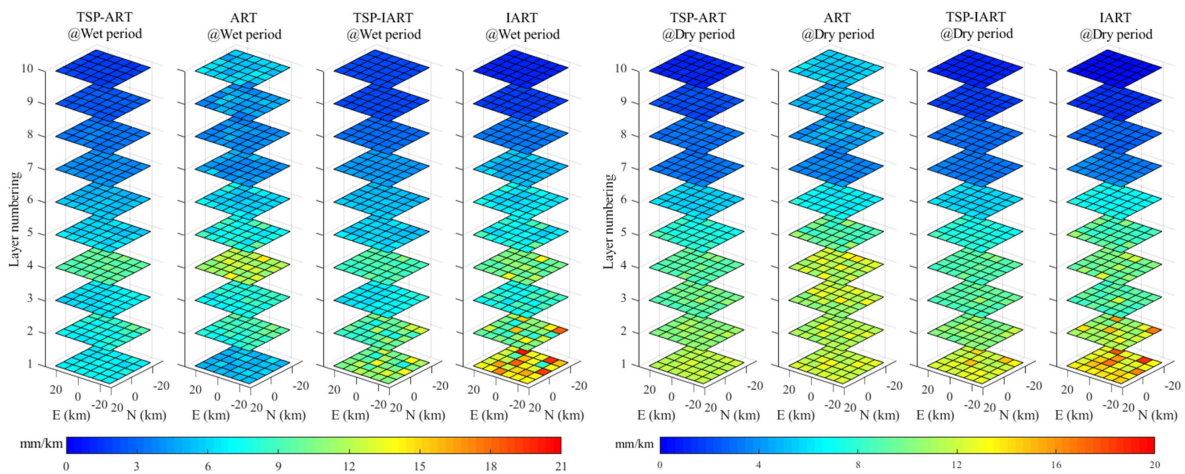

Fig. 14. RMSEs of the WR values in each voxel during the (left) wet and the (right) dry periods resulting from different algorithms for comparisons (ERA5 data were used as the reference).

TABLE III
STATISTICAL RESULTS OF WR RESULTING FROM DIFFERENT ALGORITHMS OVER THE WET AND DRY PERIODS (mm/km) (RADIOSONDE DATA WERE USED AS THE REFERENCES)

Algorithm	Wet period			Dry period		
	RMSE	MAE	Bias	RMSE	MAE	Bias
ART	7.52	5.35	−0.19	9.22	6.92	−0.72
IART	8.34	5.66	−0.46	8.71	5.46	−0.63
TSP-ART	6.79	4.70	−0.58	8.01	5.54	−1.07
TSP-IART	7.30	5.12	−0.45	7.83	5.30	−0.88
SIRT	7.38	5.24	−0.24	9.29	6.88	−0.82
ASIRT	8.38	5.66	−0.35	8.43	5.33	−0.62
TSP-SIRT	6.78	4.68	−0.67	8.06	5.57	−1.08
TSP-ASIRT	7.35	5.10	−0.41	7.78	5.28	−0.85

TABLE IV
STATISTICAL RESULTS OF THE WR VALUES OF ALL VOXELS OVER THE TWO PERIODS RESULTING FROM DIFFERENT ALGORITHMS (mm/km) (ERA5 DATA WERE USED AS THE REFERENCES)

Algorithm	Wet period			Dry period		
	RMSE	MAE	Bias	RMSE	MAE	Bias
ART	7.07	5.23	0.24	8.73	6.41	−0.31
IART	8.14	5.41	−0.11	8.17	5.08	−0.29
TSP-ART	5.92	4.27	−0.29	7.32	5.05	−0.68
TSP-IART	6.71	4.70	−0.28	7.36	4.96	−0.56
SIRT	7.17	5.24	0.36	8.85	6.39	−0.36
ASIRT	8.26	5.46	0.04	8.07	5.09	−0.20
TSP-SIRT	5.92	4.26	−0.27	7.47	5.18	−0.64
TSP-ASIRT	6.65	4.65	−0.21	7.33	4.99	−0.46

The RMSE of the WR values of all voxels on each day from different algorithms for comparison is shown in Fig. 15, where the improvement made by TPSIA is evident. Table IV shows the statistical results of all voxels during each of the two periods from each method with the ERA5 data as reference. It can be seen that the RMSEs over the wet and dry periods reduce from 7.07 and 8.73 mm/km of ART to 5.92 and 7.32 mm/km of TSP-ART, respectively, equivalent to the accuracy
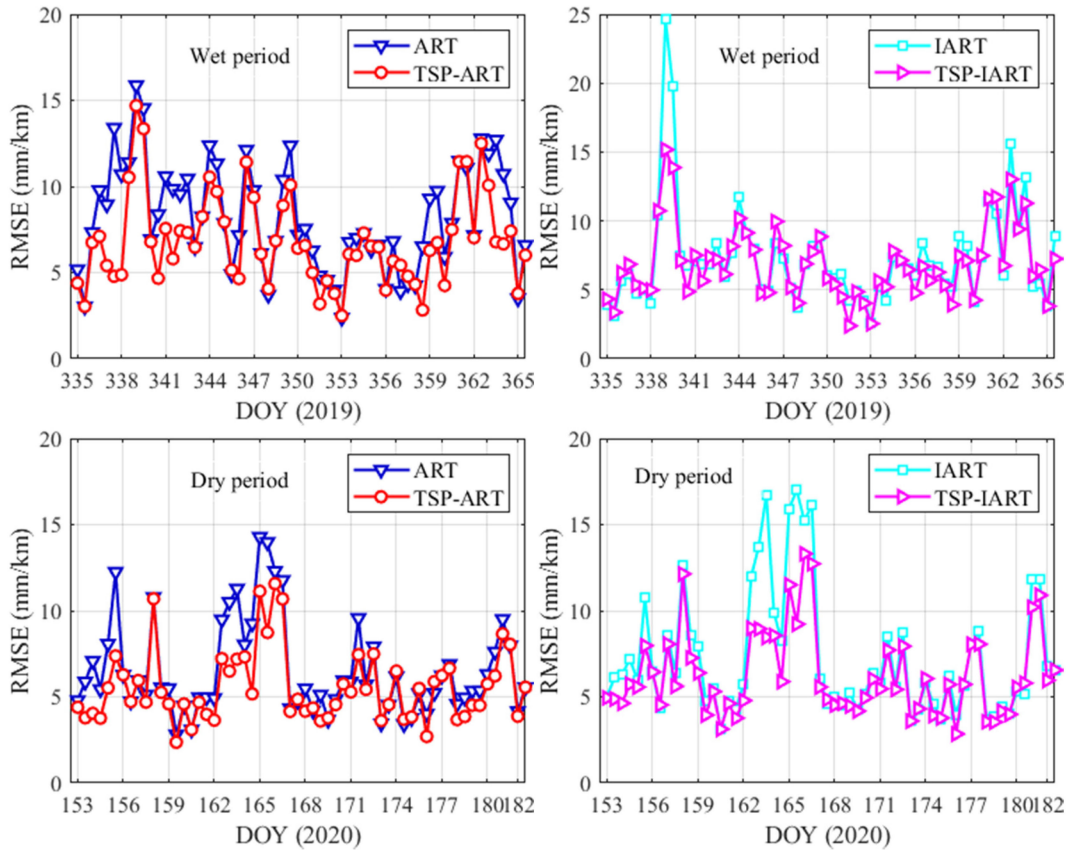
Fig. 15. RMSE of the WR values on each day during the (top) wet and the (bottom) dry periods resulting from different algorithms for comparisons (ERA5 data were used as the reference).
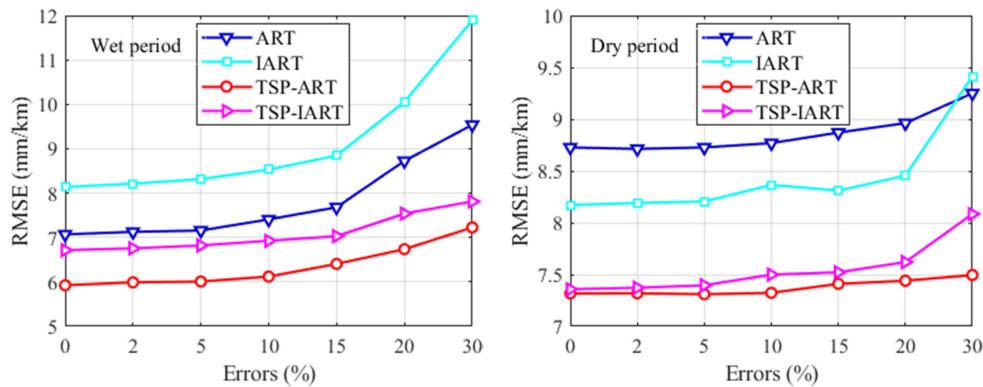

Fig. 16. RMSE of the WR values of all voxels over the (left) wet and the (right) dry periods resulting from different algorithms and from different additional errors added to the tomographic observations.

improvements of 16.27% and 16.15%; the RMSEs decrease from 8.14 and 8.17 mm/km of IART to 6.71 and 7.36 mm/km of TSP-IART, respectively, meaning improvements of 17.57% and 9.91%. All these results indicate the effectiveness of the proposed algorithm.

D. Results From Adding Additional Noise

To further test the performance of the proposed algorithm, an experiment for adding additional 2% to 30% random error to the tomographic observations (SWD) was carried out. The

ART methods were used for illustration with ERA5 data as the reference, and the other experiments setting was the same as that in Section V-C. Fig. 16 shows the RMSE of the WR values of all voxels from different algorithms and from different additional noise values added to the tomographic observations. It can be found that the proposed algorithms still significantly outperform the other two methods, and with the increase in noise, its RMSE increases (i.e., its accuracy deteriorates) smaller than the traditional methods, especially during the wet period. In addition, it is noted that when the error is under 10%, the result of classical AIR (blue) vary little with the magnitude of

the error, meaning that the accuracy of the tomographic solution from the AIR methods are stable in this error range added.

VI. Conclusion

A new method for GNSS tropospheric tomography—TSPIA was proposed in this article through which a hypothesis convex set was constructed to constrain the reconstruction in the iterations, and instead of using empirical initial values for the WR field, the initial values obtained from data preprocessing were used in tomographic system. In addition, the feature of convergence and iterative termination criteria of the AIR methods were investigated, and the 2-D-NCP criterion for water vapor tomography was applied.

The TSPIA was validated using GNSS data from the Hong Kong CORS network over both wet and dry periods, and RS and ERA5 data were used as two references. Experimental results showed that TSPIA outperformed the traditional AIR algorithms over the selected periods, and the abnormal solutions that were from the traditional algorithms were effectively improved by TSPIA. Taking the ART methods as an example, the RMSEs of WR of all voxels during the wet and the dry periods reduce from 7.52 and 9.22 mm/km of ART to 6.79 and 8.01 mm/km of TSP-ART when RS were used as the reference; these values were 7.07 and 8.73 mm/km of ART to 5.92 and 7.32 mm/km of TSP-ART when ERA5 data were used as the reference. The above results are equivalent to an improvement of 9.71% and 13.12% (using RS), as well as 16.27% and 16.15% (using ERA5 data), respectively. An experiment for the investigation of the performance of the TSPIA with additional various magnitudes of noise levels added to the tomographic observations was also carried out. Results demonstrated that TSPIA has better stability and accuracy than the traditional methods under all the noisy conditions. In addition, test results also illustrated that the introduced 2-D-NCP criterion is advantageous in terms of both computational efficiency, compared to the conventional termination criteria, and avoidance of complex work on the determination of the threshold for the termination of the iterative process.

Our future article will be investigating further improved methods and using more sources of data in the construction of a convex set, e.g., integrating some real-time external observations, including Moderate Resolution Imaging Spectroradiometer, interferometric synthetic aperture radar [57], [58], etc. Their resultant tropospheric tomography is expected to be more accurate and have great potential to apply to weather monitoring and forecasting.

References

[1] D. Perler, A. Geiger, and F. Hurter, "4D GPS water vapor tomography: New parameterized approaches," *J. Geod.*, vol. 85, pp. 539–550, 2011.

[2] C. Rocken et al., "Sensing atmospheric water vapor with the global positioning system," *Geophys. Res. Lett.*, vol. 20, no. 23, pp. 2631–2634, 2013.

[3] Q. Z. Zhao, Y. Liu, X. W. Ma, W. Q. Yao, Y. B. Yao, and X. Li, "An improved rainfall forecasting model based on GNSS observations," *IEEE Trans. Geosci. Remote Sens.*, vol. 58, no. 7, pp. 4891–4900, Jul. 2020.

[4] Q. Z. Zhao, Y. Liu, W. Q. Yao, and Y. B. Yao, "Hourly rainfall forecast model using supervised learning algorithm," *IEEE Trans. Geosci. Remote Sens.*, vol. 60, 2022, Art. no. 4100509, doi: 10.1109/TGRS.2021.3054582.

[5] Q. Z. Zhao, X. W. Ma, W. Q. Yao, Y. Liu, and Y. B. Yao, "A drought monitoring method based on precipitable water vapor and precipitation," *J. Climate*, vol. 33, no. 24, pp. 10727–10741, 2020.

[6] Q. Z. Zhao, P. F. Yang, W. Q. Yao, and Y. B. Yao, "Adaptive AOD forecast model based on GNSS-derived PWV and meteorological parameters," *IEEE Trans. Geosci. Remote Sens.*, vol. 60, 2022, Art. no. 5800610, doi: 10.1109/TGRS.2021.3099155.

[7] Q. Z. Zhao, J. Su, Z. F. Li, P. F. Yang, and Y. B. Yao, "Adaptive aerosol optical depth forecasting model using GNSS observation," *IEEE Trans. Geosci. Remote Sens.*, vol. 60, 2022, Art. no. 4105009, doi: 10.1109/TGRS.2021.3129159.

[8] A. Flores, G. Ruffini, and A. Rius, "4D tropospheric tomography using GPS slant wet delays," *Ann. Geophys.*, vol. 18, no. 2, pp. 223–234, 2000.

[9] C. Champollion et al., "GPS water vapour tomography: Preliminary results from the ESCOMPTE field experiment," *Atmos. Res.*, vol. 74, no. 1–4, pp. 253–274, 2005.

[10] M. C. Zhu, Z. Z. Liu, and W. S. Hu, "Observing water vapor variability during three super typhoon events in Hong Kong based on GPS water vapor tomographic modeling technique," *J. Geophys. Res.-Atmos.*, vol. 125, no. 15, 2020, Art. no. e2019JD032318.

[11] W. X. Zhang et al., "Rapid troposphere tomography using adaptive simultaneous iterative reconstruction technique," *J. Geod.*, vol. 94, no. 8, 2020, Art. no. 94.

[12] K. F. Zhang, T. Manning, S. Q. Wu, W. Rohm, D. Silcock, and S. Choy, "Capturing the signature of severe weather events in Australia using GPS measurements," *IEEE J. Sel. Topics Appl. Earth Observ. Remote Sens.*, vol. 8, no. 4, pp. 1839–1847, Apr. 2015.

[13] Z. H. Xiong, B. Zhang, and Y. B. Yao, "Comparisons between the WRF data assimilation and the GNSS tomography technique in retrieving 3-D wet refractivity fields in Hong Kong," *Ann. Geophys.*, vol. 37, no. 1, pp. 25–36, 2019.

[14] W. Rohm and J. Bosy, "The verification of GNSS tropospheric tomography model in a mountainous area," *Adv. Space Res.*, vol. 47, no. 10, pp. 1721–1730, 2011.

[15] M. Troller et al., "Tomographic determination of the spatial distribution of water vapor using GPS observations," *Adv. Space Res.*, vol. 37, no. 12, pp. 2211–2217, 2006.

[16] W. Rohm, "The ground GNSS tomography—Unconstrained approach," *Adv. Space Res.*, vol. 51, no. 3, pp. 501–513, 2013.

[17] M. J. Shafei and M. M. Hossainali, "Application of the GPS reflected signals in tomographic reconstruction of the wet refractivity in Italy," *J. Atmos. Sol.-Terr. Phys.*, vol. 207, 2020, Art. no. 105348.

[18] A. Sa, W. Rohm, R. M. Fernandes, E. Trzcina, M. Bos, and F. Bento, "Approach to leveraging real-time GNSS tomography usage," *J. Geod.*, vol. 95, no. 8, 2021, Art. no. 1464.

[19] B. Chen and Z. Liu, "Voxel-optimized regional water vapor tomography and comparison with radiosonde and numerical weather model," *J. Geod.*, vol. 88, no. 7, pp. 691–703, 2014.

[20] R. Gordon, R. Bender, and G. T. Herman, "Algebraic reconstruction techniques (ART) for three-dimensional electron microscopy and X-ray photography," *J. Theor. Biol.*, vol. 29, no. 3, pp. 471–481, 1970.

[21] P. Gilbert, "Iterative methods for the three-dimensional reconstruction of an object from projections," *J. Theor. Biol.*, vol. 36, no. 1, pp. 105–117, 1972.

[22] D. B. Wen, Y. B. Yuan, J. K. Ou, X. L. Huo, and K. F. Zhang, "Three-dimensional ionospheric tomography by an improved algebraic reconstruction technique," *GPS Solutions*, vol. 11, no. 4, pp. 251–258, 2007.

[23] Y. B. Yao, J. Tang, L. Zhang, C. Y. He, and S. Zhang, "An adaptive simultaneous iteration reconstruction technique for three-dimensional ionospheric tomography," *Chin. J. Geophys.*, vol. 57, no. 2, pp. 345–353, 2014.

[24] P. Xia, C. Cai, and Z. Liu, "GNSS troposphere tomography based on two-step reconstructions using GPS observations and COSMIC profiles," *Ann. Geophys.*, vol. 31, no. 10, pp. 1805–1815, 2013.

[25] M. Bender et al., "Development of a GNSS water vapour tomography system using algebraic reconstruction techniques," *Adv. Space Res.*, vol. 47, no. 10, pp. 1704–1720, 2011.

[26] X. Y. Wang, Z. G. Dai, E. H. Zhang, K. E. Fuyang, Y. C. Cao, and L. C. Song, "Tropospheric wet refractivity tomography using multiplicative algebraic reconstruction technique," *Adv. Space Res.*, vol. 53, no. 1, pp. 156–162, 2014.

[27] S. Z. Liu, J. X. Wang, and J. Q. Gao, "Inversion of ionospheric electron density based on a constrained simultaneous iteration reconstruction technique," *IEEE Trans. Geosci. Remote Sens.*, vol. 48, no. 6, pp. 2455–2459, Jun. 2010.

[28] D. B. Wen, S. Z. Liu, and P. Y. Tang, "Tomographic reconstruction of ionospheric electron density based on constrained algebraic reconstruction technique," *GPS Solutions*, vol. 14, no. 4, pp. 375–380, 2010.

[29] Y. B. Yao, C. Z. Zhai, J. Kong, C. J. Zhao, Y. Y. Luo, and L. Liu, "An improved constrained simultaneous iteration reconstruction technique for ionospheric tomography," *GPS Solutions*, vol. 24, no. 3, pp. 2455–2459, 2020.

[30] Z. Adavi, R. Weber, and M. F. Glaner, "Assessment of regularization techniques in GNSS tropospheric tomography based on single- and dual-frequency observations," *GPS Solutions*, vol. 26, 2022, Art. no. 21.

[31] Y. B. Yao, J. Tang, P. Chen, S. Zhang, and J. J. Chen, "An improved iterative algorithm for 3-D ionospheric tomography reconstruction," *IEEE Trans. Geosci. Remote Sens.*, vol. 52, no. 8, pp. 4696–4706, Aug. 2014.

[32] F. V. Salina, N. D. A. Mascarenhas, and P. E. Cruvinel, "A comparison of POCS algorithms for tomographic reconstruction under noise and limited view," in *Proc. 15th Braz. Symp. Comput. Graph. Image Process.*, 2002, pp. 342–346.

[33] T. Elfving, P. C. Hansen, and T. Nikazad, "Semiconvergence and relaxation parameters for projected SIRT algorithms," *SIAM J. Sci. Comput.*, vol. 34, no. 4, pp. A2000–A2017, 2012.

[34] M. Bertero, D. Bindi, P. Boccacci, M. Cattaneo, C. Eva, and V. Lanza, "Application of the projected landweber method to the estimation of the source time function in seismology," *Inverse Problems*, vol. 13, no. 2, 1997, Art. no. 465.

[35] F. Benvenuto, R. Zanella, L. Zanni, and M. Bertero, "Nonnegative least-squares image deblurring: Improved gradient projection approaches," *Inverse Problems*, vol. 26, no. 2, 2010, Art. no. 025004.

[36] J. N. Hao, W. L. Yin, Q. Zhao, K. Xu, and G. Chen, "Preconditioning of projected SIRT algorithm for electromagnetic tomography," *Flow Meas. Instrum.*, vol. 29, pp. 39–44, 2013.

[37] Z. H. Meng, W. Li, F. T. Li, and H. Y. Li, "Projected Barzilai–Borwein method for the acceleration of gravity field data inversion," *Explor. Geophys.*, vol. 52, pp. 356–367, 2021.

[38] Y. Sui et al., "Sparse reconstruction of 3-D regional ionospheric tomography using data from a network of GNSS reference stations," *IEEE Trans. Geosci. Remote Sens.*, vol. 60, 2022, Art. no. 4102615, doi: 10.1109/TGRS.2021.3087789.

[39] W. Y. Zhang, S. B. Zhang, G. B. Chang, N. Ding, and X. M. Wang, "A new hybrid observation GNSS tomography method combining the real and virtual inverted signals," *J. Geod.*, vol. 95, 2021, Art. no. 128.

[40] W. X. Liu, Y. D. Lou, W. X. Zhang, J. F. Huang, Y. Z. Zhou, and H. S. Zhang, "On the study of influences of different factors on the rapid tropospheric tomography," *Remote Sens.*, vol. 11, no. 13, 2019, Art. no. 1545.

[41] P. C. Hansen, "Getting to business: Discretizations of linear inverse problems," in *Discrete Inverse Problems: Insight and Algorithms*, P. C. Hansen, Ed. Philadelphia, PA, USA: SIAM, 2010, pp. 23–48.

[42] J. Saastamoinen, "Atmospheric correction for troposphere and stratosphere in radio ranging of satellites," in *The Use of Artificial Satellites For Geodesy*, vol. 15, S. W. Henriksen, A. Macini, and B. H. Chovitz, Eds. Washington, DC, USA: American Geophysical Union, 1972, pp. 247–251.

[43] M. Bevis, S. Businger, T. A. Herring, C. Rocken, R. A. Anthes, and R. H. Ware, "GPS meteorology: Remote sensing of atmospheric water vapor using the global positioning system," *J. Geophys. Res. Atmos.*, vol. 97, no. D14, pp. 15787–15801, 1992.

[44] V. Mendes, "Modeling the neutral-atmospheric propagation delay in radiometric space techniques," Ph.D. dissertation, Dept. Geodesy Geomatics Eng., Univ. New Brunswick, Fredericton, New Brunswick, Canada, 1999.

[45] S. Karczmarz, "Angenaherte auflosung von systemen linearer gleichungen," *Bull. Int. de l' Académie Polonaise des Sci. et des Lettres*, vol. 35, pp. 355–357, 1937.

[46] G. Cimmino, "Calcolo approsimato per le soluzioni dei sistemi di equazionii lineari," *La Ricerca Scientifica*, vol. 9, pp. 326–333, 1938.

[47] P. C. Hansen and J. S. Jorgensen, "AIR tools II: Algebraic iterative reconstruction methods, improved implementation," *Numer. Algorithms*, vol. 79, no. 1, pp. 107–137, 2018.

[48] T. Elfving, P. C. Hansen, and T. Nikazad, "Semi-convergence properties of Kaczmarz's method," *Inverse Problems*, vol. 30, no. 5, 2014, Art. no. 055007.

[49] T. Elfving, T. Nikazad, and P. C. Hansen, "Semi-convergence and relaxation parameters for a class of SIRT algorithms," *Electron. Trans. Numer. Anal.*, vol. 37, pp. 321–336, 2010.

[50] W. Rohm, "The precision of humidity in GNSS tomography," *Atmos. Res.*, vol. 107, pp. 69–75, 2012.

[51] R. Dach and P. Walser, *Bernese GNSS Software Version 5.2*. Bern, Switzerland: Astronomical Institute, Univ. Bern, 2013.

[52] J. Boehm, A. Niell, P. Tregoning, and H. Schuh, "Global mapping function (GMF): A new empirical mapping function based on numerical weather model data," *Geophys. Res. Lett.*, vol. 33, no. 7, pp. L07304–1–L07304–4, 2006.

[53] P. C. Hansen, M. E. Kilmer, and R. H. Kjeldsen, "Exploiting residual information in the parameter choice for discrete ill-posed problems," *Bit*, vol. 46, no. 1, pp. 41–59, 2006.

[54] B. W. Rust and D. P. O'Leary, "Residual periodograms for choosing regularization parameters for ill-posed problems," *Inverse Problems*, vol. 24, no. 3, 2008, Art. no. 034005.

[55] H. E. Lin, L. Lintao, S. U. Xiaoqing, X. U. Chaoqian, and D. Pengshuo, "Algebraic reconstruction algorithm of vapor tomography," *Acta Geodaetica et Cartographica Sinica*, vol. 44, no. 1, 2015, Art. no. 32.

[56] B. Zhang, Q. Fan, Y. Yao, C. Xu, and X. Li, "An improved tomography approach based on adaptive smoothing and ground meteorological observations," *Remote Sens.*, vol. 9, no. 9, 2017, Art. no. 886.

[57] W. Zhang, S. Zhang, N. Zheng, N. Ding, and X. Liu, "A new integrated method of GNSS and MODIS measurements for tropospheric water vapor tomography," *GPS Solutions*, vol. 25, no. 2, 2021, Art. no. 79.

[58] M. Heublein, F. Alshawaf, B. Erdnuess, X. X. Zhu, and S. Hinz, "Compressive sensing reconstruction of 3D wet refractivity based on GNSS and InSAR observations," *J. Geod.*, vol. 93, no. 2, pp. 197–217, 2019.

Shangyi Liu received the B.Sc. degree in surveying engineering from the School of Geodesy and Geomatics, Wuhan University, Wuhan, China, in 2020. He is currently working toward the M.S. degree in surveying and mapping engineering with the School of Environment Science and Spatial Informatics, China University of Mining and Technology, Xuzhou, China.

His research interests include global navigation satellite system meteorology.

Kefei Zhang received the Ph.D. degree in geodesy from the Curtin University, Perth, WA, Australia, in 1998.

He is currently a Chair Professor and the Director of the Institute of Resources and Environment Technologies, University of Mining and Technology (CUMT), Tarkwa, China. He is also a Honorary Professor with the RMIT University, Melbourne, VIC, Australia, where he is the Founding Director of the Satellite Positioning for Atmosphere, Climate and Environment Research Centre. He has more than 30 years of research experience in geodesy, satellite positioning, and geospatial sciences in general. He has authored about 400 peer-reviewed publications in these fields and a coinventor of 30 patents, and attracted in excess of 50 million dollars in funding from the Australian Research Council, National Science Foundation of China, as well as funds from other national and international governments and industries. He is an Australian Pioneer in cutting-edge technologies for smart tracking, GNSS atmospheric sounding for weather and climate, and space environment management. His satellite-to-satellite tracking frontier research has led to more than 10-h weather forecast improvement and successful integration of the GPS radio occultation data into the Australian weather forecasting system in 2012. He currently leads a team of more than 40 researchers with the CUMT. His research interests include algorithm development and innovative applications of satellite technologies for high-accuracy positioning, atmospheric studies, space situational awareness, and space resources utilization. He is fellow of The International Association of Geodesy (IAG).

Suqin Wu received the Ph.D. degree in regional atmospheric modelling for network-RTK from RMIT University, Melbourne, VIC, Australia, in 2009.

She is currently a Professor with the China University of Mining and Technology, Beijing, China. Her research interests include GNSS precise positioning and GNSS meteorology, GPS radio occultation, atmospheric error modeling for high accuracy GNSS applications, and precise orbit determination and prediction for space debris objects.

Jiaqi Shi received the B.Sc. degree in surveying engineering from the School of Geodesy and Geomatics, Wuhan University, Wuhan, China, in 2019. He is currently working toward the M.S. degree in geodesy and surveying engineering with the School of Environment Science and Spatial Informatics, China University of Mining and Technology, Xuzhou, China.

His research interests include radio occultation, GNSS meteorology, and precise point positioning.

Wenyuan Zhang received the B.Sc. degree in surveying engineering from the China University of Mining and Technology, Xuzhou, China, in 2018. He is currently working toward the Ph.D. degree in geodesy and surveying engineering with the School of Environment Science and Spatial Informatics, China University of Mining and Technology, Xuzhou, China.

His research interests include global navigation satellite system meteorology as well as innovative models and algorithms for tropospheric tomography.

Minghao Zhang received the B.Sc. degree in surveying engineering from the China University of Mining and Technology, Xuzhou, China, in 2020, where he is currently working toward the Ph.D. degree in geodesy and surveying engineering with the School of Environment Science and Spatial Informatics.

His research interests include global navigation satellite system meteorology.

Longjiang Li received the B.Sc. degree in surveying engineering from the China University of Mining and Technology, Xuzhou, China, in 2018. He is currently working toward the Ph.D. degree in geodesy and geomatics engineering with the China University of Mining and Technology, Xuzhou, China.

His research interests include retrieval of PWV from GNSS observation and its application in extreme weather forecast.

Moufeng Wan received the B.Sc. and M.S. degrees in surveying engineering from the China University of Mining and Technology, Beijing, China, in 2009 and 2012, respectively, where he is currently working toward the Ph.D. degree in geodesy and surveying engineering with the School of Environment Science and Spatial Informatics.

He has been active in nonlinear Kalman Filter and its applications in GNSS data processing and statistical theory and its applications in GNSS. His research interests include GNSS tomography, four-dimensional atmospheric water vapor modeling, and meteorological applications of GNSS.
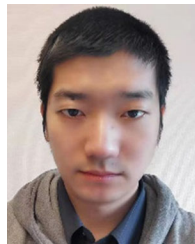
Andong Hu received the Ph.D. degree in geospatial science from the Royal Melbourne Institute of Technology, Melbourne, VIC, Australia, in 2020.

He is currently working as a Postdoc with the CU Boulder and the NOAA Space Weather Prediction Center. His research interests include machine learning algorithm development and innovative applications of space weather modeling for solar wind prediction, solar wind, and magnetosphere coupling, and ionosphere analysis.